Optics Letters

Atmospheric effects on the laser-driven avalanche-based remote detection of radiation

A. Zingale,[1,2,*] S. Waczynski,[1] J. Sears,[3] R. E. Lakis,[2] and H. M. Milchberg[1]

[1]Institute for Research in Electronics and Applied Physics, University of Maryland, College Park, Maryland 20742, USA
[2]Los Alamos National Laboratory, Los Alamos, New Mexico 87545, USA
[3]Lawrence Livermore National Laboratory, Livermore, California 94550, USA
*azingale@umd.edu

Received 21 February 2023; revised 30 March 2023; accepted 6 April 2023; posted 7 April 2023; published 1 May 2023

The effect of realistic atmospheric conditions on mid-IR ($\lambda = 3.9\,\mu m$) and long-wave-IR ($\lambda = 10\,\mu m$) laser-induced avalanche breakdown for the remote detection of radioactive material is examined experimentally and with propagation simulations. Our short-range in-lab mid-IR laser experiments show a correlation between increasing turbulence level and a reduced number of breakdown sites associated with a reduction in the portion of the focal volume above the breakdown threshold. Simulations of propagation through turbulence are in excellent agreement with these measurements and provide code validation. We then simulate propagation through realistic atmospheric turbulence over a long range (0.1–1 km) in the long-wave-IR regime ($\lambda = 10\,\mu m$). The avalanche threshold focal volume is found to be robust even in the presence of strong turbulence, only dropping by ~50% over a propagation length of ~0.6 km. We also experimentally assess the impact of aerosols on avalanche-based detection, finding that, while background counts increase, a useful signal is extractable even at aerosol concentrations 10^5 times greater than what is typically observed in atmospheric conditions. Our results show promise for the long-range detection of radioactive sources under realistic atmospheric conditions.

https://doi.org/10.1364/OL.488346

Remote stand-off detection of radioactive materials is an area of increasing interest [1–5]. Radioactive decay typically involves the emission of high-energy alpha particles, beta particles, or gamma rays (i.e., photons). The unshielded ranges in air of these radiations scale from a few centimeters to over 100 meters. Traditional near-field detectors sense these emissions by intercepting them along their path lengths. However, because the flux of decay particles drops rapidly with distance owing to geometric falloff and scattering losses, particle/photon detectors must be placed relatively close to the source. The decay particles also ionize the air near the source, but this excess ionization also drops rapidly with distance. Recent experiments have demonstrated the detection of radioactive materials at meter-scale stand-off distances in the lab using a mid-IR laser-induced electron avalanche, which drives the amplification of the excess ionization to levels measurable by remote detectors while suppressing multiphoton ionization seeding of the avalanche by the laser pulse itself [2,6]. In another approach, a 95 GHz gyrotron was used as the avalanche driver [5], but rapid diffraction of such long-wavelength beams makes these methods less practical than lasers.

Avalanche breakdown of air occurs when the electric field in the focal region of an intense laser pulse accelerates a free electron, driving collisions with neutral air molecules, leading to resistive heating and further collisional ionization. This exponentially increases the number of free electrons until the process saturates at a final plasma density that can be measured by a variety of diagnostics at range.

In order to extend this technique well beyond the meter range in the lab to hundreds of meters in the atmosphere, one must understand the effect of realistic atmospheric conditions on long-range laser propagation and avalanche breakdown. The topic of light propagation in atmospheric turbulence has been widely studied, with applications such as optical communications, remote sensing, and imaging of astronomical objects [7–10]. Here, we are interested in mid-IR and long-wave-IR pulses tens of picoseconds in duration that are focused through turbulent air (with possible aerosol content) to drive radioactive-source-seeded avalanche breakdown. To explore the dependence of the breakdown on atmospheric conditions, we performed experiments with controlled turbulence over a short range in the lab. These experiments were used to benchmark propagation simulations, which were then extended to long-range realistic atmospheric conditions. We also tested the effect of aerosols in the focal volume.

The experimental setup is shown in Fig. 1. Mid-IR avalanche driver pulses with $\lambda = 3.9\,\mu m$ (0.32 eV), energy < 10 mJ, 70 ps full width at half maximum (FWHM) uncompressed pulses generated by an optical parametric chirped pulse amplification (OPCPA) system at the University of Maryland [1,2,11] were triple-passed with a beam diameter of ~12 mm or 25 mm through a heater-controlled turbulence cell. The total path length through the cell was 50 cm. The beam was then focused by a 250 mm focal length ($f/10$) lens to a waist ~3 cm from a 2.5 mCi Po-210 α-particle source. The 5.3 MeV α-particles have a ~3 cm range in air. As they collide with air molecules and deposit energy, they liberate electrons, which rapidly attach to oxygen molecules on a 70 ns time scale [12], forming O_2^- molecular ions [13]. With a

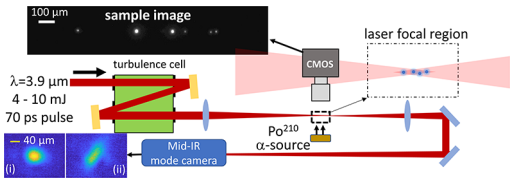

Fig. 1. Experimental layout. A λ = 3.9 μm, 4–10 mJ, 70 ps FWHM duration pulse is triple-passed through a controlled turbulence cell of total path 50 cm and focused by a 250 mm focal length lens ($f/20$) to a waist 3 cm from a ∼1 mCi Po-210 α-particle source. The 5.3 MeV α-particle interaction with air provides seed electrons and weakly bound negative ions for avalanche breakdown. Recombination light from breakdown plasma balls seeded by individual electrons is imaged with a CMOS camera. An infrared camera is used to image the focus of the λ = 3.9 μm beam at its waist in the interaction volume: (i) focal spot image with the turbulence cell heater off; (ii) typical image with the heater on ($C_n^2 = 2 \times 10^{-9}$ m$^{-2/3}$).

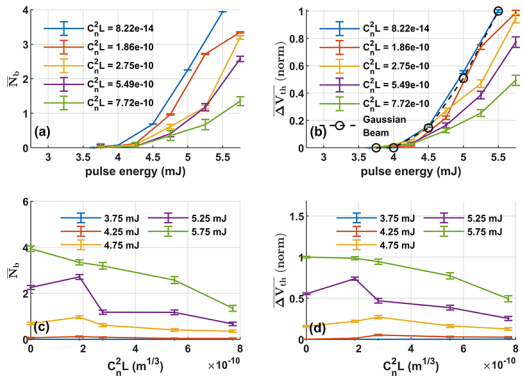

Fig. 2. (a) Plot of $\overline{N_b}$ (number of breakdown sites per shot, averaged over a 200-shot set) versus the laser pulse energy for varying turbulence level. (b) Plot of $\overline{\Delta V_{th}}$ (200-shot average focal volume above the breakdown threshold) versus the laser pulse energy for varying turbulence level. Open circles plot ΔV_{th} for a 72 μm FWHM Gaussian beam waist with $I_{th} = 10^{12}$ W/cm^2. (c) $\overline{N_b}$ versus the turbulence level for varying pulse energy. (d) $\overline{\Delta V_{th}}$ versus the turbulence level for varying pulse energy. Error bars indicate the standard error for all points.

low binding energy of ∼0.46 eV, O_2^- is readily two-photon ionized to produce free electrons early in the mid-IR laser pulse [2]. Individual free electrons then serve as seeds for electron avalanche breakdown, which forms localized plasma balls [6] whose recombination fluorescence is imaged with a complementary metal-oxide semiconductor (CMOS) camera. The number of plasma balls in each image is therefore proportional to the seed density in the focal volume. The focus of the λ = 3.9 μm beam is imaged by a FLIR A6780 mid-wave infrared (MWIR) camera.

The turbulence cell consists of a hot plate at the base of an open-top box with apertures for the mid-IR beam to pass through (see Fig. 1). Varying the hot plate temperature controls the turbulence strength in the cell [14]. The turbulence strength was quantified by measuring the refractive index structure parameter C_n^2 as a function of hot plate temperature. To do this, a λ = 532 nm continuous-wave (CW) diode probe beam was propagated along the path of the 3.9 μm beam through the turbulence cell, followed by a 4.25 m path in lab air to a camera. The angular deflection θ (rad) of the probe on the camera is related to the structure parameter by $C_n^2 L = \theta^2 D^{1/3}/2.91$ [15], where D is the beam diameter and $L = 50$ cm is the path length through the turbulence. For the range of hot plate temperatures used, C_n^2 was controlled between 10^{-10} m$^{-2/3}$ and 2×10^{-9} m$^{-2/3}$, far exceeding the typical atmospheric turbulence range of $10^{-17} - 10^{-13}$ m$^{-2/3}$ [16]. However, the path-length-integrated turbulence $C_n^2 L$ in our cell is of the same order as strong atmospheric turbulence ($C_n^2 \sim 10^{-13} - 10^{-12}$) and the propagation length ∼1 km.

We investigated the effect of turbulence on avalanche breakdown by directly counting the number N_b of breakdown sites produced by each shot, as shown in the sample image of Fig. 1. Scans were taken over pulse energy and turbulence level, as plotted in Fig. 2, with 200 shots taken for each point. We first imaged the beam focal spot and recorded I_{th}, the signal count of its highest-intensity pixel at the air breakdown threshold (3.75 mJ for the appearance of an average of ∼1 breakdown site per 20 shots) in the presence of the Po-210 with the turbulence cell heater off. For all higher-energy shots with and without the cell heater on, we define the "above breakdown threshold area" of the beam as $\Delta A_{th} = \sum_{I_{pix} > I_{th}} I_{pix}$; that is, the total number of pixels in the focal spot image with intensity $I_{pix} > I_{th}$. A very good estimate of the effective volume in the laser focus above the breakdown threshold is then $\Delta V_{th} \propto \Delta A_{th}$.

Figures 2(a) and 2(b) respectively plot the 200-shot averages $\overline{N_b}$ and $\overline{\Delta V_{th}}$ as a function of pulse energy for varying turbulence strength, and Figs. 2(c) and 2(d) plot them as a function of turbulence strength for varying pulse energy. In general, increased turbulence reduces both $\overline{N_b}$ and $\overline{\Delta V_{th}}$ for a given pulse energy, as seen in Figs. 2(a) and 2(b). The reduction in $\overline{\Delta V_{th}}$ reflects the reduction in pixel intensity I_{pix} from turbulence-induced focal spot distortion. Interestingly, for the lower pulse energies we see a slight increase in $\overline{N_b}$ in the turbulence range $C_n^2 L = 2 - 3 \times 10^{-10}m^{1/3}$, followed by a decrease at higher turbulence levels [see Fig. 2(c)]. Similar behavior is followed by $\overline{\Delta V_{th}}$ in Fig. 2(d). This suggests that at lower pulse energies, small phase perturbations from the turbulence can actually create hot spots in the beam that increase $\overline{\Delta V_{th}}$ and thus $\overline{N_b}$. At the highest energy, 5.75 mJ, this trend disappears and there is a monotonic decrease in breakdown sites with increasing turbulence strength. As a check on our procedure, in Fig. 2(b) we plot the calculated focal volume above threshold (∼ 1 TW/cm^2 [1,6] for a λ = 3.9 μm, 70 ps pulse) for a Gaussian beam with a 72 μm FWHM beam waist (open circles and dashed line), which closely tracks the curve for $\overline{\Delta V_b}$ at the lab background turbulence level ($C_n^2 L = 8.22 \times 10^{-14}m^{1/3}$).

We note that the results of Fig. 2 demonstrate considerable robustness of laser-driven avalanche detection in the presence of strong turbulence: at the highest turbulence level of $C_n^2 L = 8 \times 10^{-10}m^{1/3}$, i.e., 4 orders of magnitude higher than the lab background level ($C_n^2 L = 8 \times 10^{-14}m^{1/3}$), only a ∼20% increase in laser energy is needed to generate the same number of breakdown sites.

We also investigate the effect of aerosols in the focal volume with the turbulence cell turned off. The aerosol particles were generated with a commercial nebulizer submerged in water, producing droplets with ∼5 μm average diameter [17]. Each aerosol particle is assumed to produce a breakdown owing to a significantly lower breakdown intensity threshold. In the case of

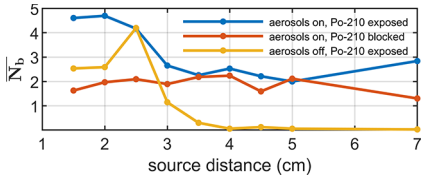

Fig. 3. Plot of $\overline{N_b}$ versus the α-source-to-focus distance for the conditions shown in the plot legend.

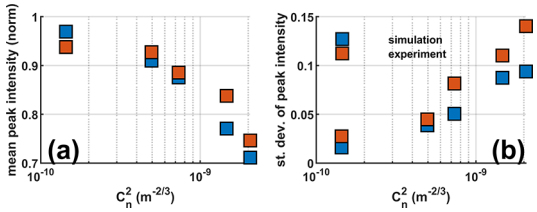

Fig. 4. (a) Simulated mean peak intensity $\overline{I_{peak}}$ (over 200 simulation runs) and experimental mean peak intensity $\overline{I_{pix,peak}}$ (over 200 shots). Points are normalized to the maximum single run or shot values. (b) Corresponding standard deviations.

Ref. [18], the threshold was reduced from 10^9 W/cm^2 for clean air to $<10^6$ W/cm^2 for aerosol-contaminated air. Figure 3 plots $\overline{N_b}$ as a function of Po-210 α-particle-source-to-focal-volume distance with a pulse energy of 5 mJ for three cases: aerosol generator on and α-source exposed, aerosol generator on and α-source blocked, and aerosol generator off and Po-210 source exposed. Not unexpectedly, the general effect of the aerosols is to increase $\overline{N_b}$ independent of the source-to-focus distance. With the aerosol generator off, $\overline{N_b}$ is near zero at distances > 4 cm. For α-source-to-focus distances <3 cm, the Po-210 still seeds enough breakdowns to be detectable above the aerosol-induced background.

The nominal focal volume for the 72 μm FWHM focal spot with a ∼500 μm Rayleigh range is $\sim 2 \times 10^{-6}$ cm^3, meaning that the aerosol-induced background density observed (2 breakdowns per shot) was $\sim 10^6$ cm^{-3}. This far exceeds typical atmospheric aerosol concentrations. For instance, the air quality index (AQI) measures particulate contamination in air ranging from "good" (0 AQI) to "hazardous" (500 AQI) air quality. Assuming the density of water and spherical particles of 2.5 μm diameter, an AQI of 500 corresponds to ∼10 cm^{-3}, 5 orders of magnitude lower than the concentration in our experiment and at least an order of magnitude lower than typical background ion densities in air ($10^2 - 10^3$ cm^{-3} [2,6]). This strongly suggests that aerosols will not play a dominant role in typical outdoor conditions.

Simulations of mid-IR laser pulse propagation and focusing in atmospheric turbulence were performed [19] to (1) validate the code against the results of our in-lab measurements and then (2) simulate the effect of turbulence on avalanche-based detection at kilometer propagation distances. Turbulence was simulated using multiple 2D phase screens [20] generated by Fourier filtering random noise with a modified von Kármán spectrum [21], followed by an inverse transform into the spatial domain. An inner scale of 1 mm and an outer scale of 1 m were used [14]. The number of phase screens was balanced between acceptable accuracy and a reasonable computation time. Ideally, the distance between screens would approach zero because the medium being modeled is continuous. We define acceptable accuracy as following the condition that the variance of relative intensity fluctuations due to a single screen is always less than 0.1. Therefore, the contribution of each screen is weak. This practical condition corresponds to having a total number of phase screens above $(10\sigma_R^2)^{6/11}$, where σ_R^2 is the Rytov variance [22].

For validating the code against our experiment, we simulated the propagation of a $\lambda = 3.9$ μm, 70 ps duration, $w_0 = 6$ mm ($1/e^2$ intensity radius) Gaussian beam from its waist through 50 cm of turbulence, with C_n^2 ranging between 10^{-10} and 2×10^{-9} m$^{-2/3}$, corresponding to Fig. 2. The phase screens were placed every 5 cm within the turbulent region. Upon exiting the turbulence, the beam was propagated 25 cm to a $f/10$ lens and then to focus. The peak intensity I_{peak} in the focal volume was extracted for each of 200 simulation runs at each turbulence level, with the mean $\overline{I_{peak}}$ and standard deviation at each level plotted in Fig. 4. It is seen that the $\overline{I_{peak}}$ points compare quite well with the mean values $\overline{I_{pix,peak}}$ from the experiment, where $I_{pix,peak}$ is the peak intensity on each of 200 shots, as measured by the focal spot camera (arb. units). The simulated and experimental standard deviations also agree reasonably well, albeit with a slight underestimate by the simulation.

Considering the results of Fig. 4 as a validation of the simulation code, we then simulated a more realistic propagation geometry in the atmosphere. We select a λ = 10 μm, 15 J energy, 70 ps duration pulse because there are no currently available multi-joule mid-IR sources, but CO_2 lasers that provide joule-level pulses of picosecond-scale duration are available [23] and can realistically reach the avalanche breakdown threshold at significant range [6]. We note that these simulations do not include nonlinear propagation effects, so the accuracy of the results degrades as the laser pulse power approaches and exceeds the critical power for self-focusing, P_{cr}. Here, the simulated pulse power is $\sim P_{cr}/3$, well within the range for linear propagation. The propagation simulation is initialized by imparting a concave, spherical phase profile, and the focal length and initial beam diameter are varied to maintain a constant $f/1000$ focusing geometry, which gives a constant focal volume and peak intensity for the case of no turbulence. This enables straightforward analysis of ΔV_{th} and I_{peak} for varying conditions. Here, for λ = 10 μm, we take $I_{th} = 0.15$ TW/cm^2, using the λ^2 scaling for laser heating and the known threshold $\sim 10^{12}$ W/cm^2 at λ = 3.9 μm [1,6].

Typical values of C_n^2 near ground level vary from $\sim 10^{-17}$ m$^{-2/3}$ for "weak" turbulence to $\sim 10^{-13}$ m$^{-2/3}$ for "strong" turbulence [16]. We simulate these extreme cases for focusing distances between 100 m and 1000 m. The results are shown in Fig. 5. For weak turbulence [Fig. 5(a)], even for focusing at 1000 m, there is no significant effect on I_{peak} or ΔV_{th}. For strong turbulence [Fig. 5(b)], there is a steady decline in I_{peak} and ΔV_{th}, with the latter dropping by a factor of ∼2 at 600 m.

Finally, we can unify our in-lab experimental results with the long-range propagation simulations by plotting I_{peak} and ΔV_{th} as a function of $C_n^2 L$, where L is the propagation length in turbulent air. In the experiment, $C_n^2 L \sim 10^{-10}$m$^{1/3}$ (see Fig. 2) with comparatively small L. Another set of simulations was conducted determining I_{peak} and ΔV_{th} over 5 values of C_n^2 for each of 6 values of L, yielding a range of $C_n^2 L$ spanning ∼5 orders of magnitude. Figures 5(c) and 5(d) plot the normalized results of these simulations with normalized experimental values superposed. These results suggest a general threshold of $C_n^2 L \sim 10^{-10}$m$^{1/3}$ above

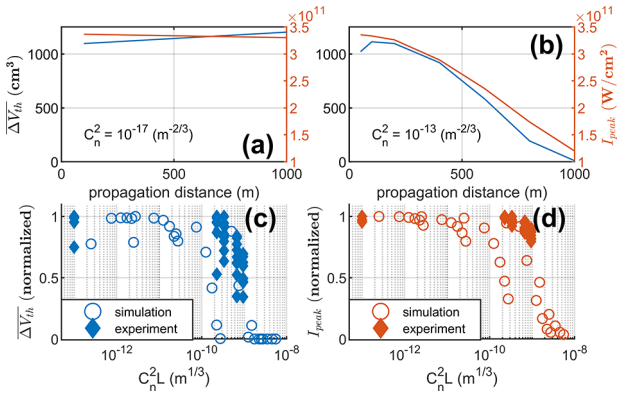

Fig. 5. (a) Simulated ΔV_{th} and I_{peak} versus the propagation distance for $C_n^2 = 10^{-17}\mathrm{m}^{-2/3}$. (b) The same for $C_n^2 = 10^{-13}\mathrm{m}^{-2/3}$. (c) Simulated and experimental ΔV_{th} versus $C_n^2 L$. (d) Simulated and experimental I_{peak} versus $C_n^2 L$.

which ΔV_{th} and I_{peak} undergo significant degradation. Between 10^{-10} and $10^{-9}\mathrm{m}^{1/3}$, there is almost 100% variation for both ΔV_{th} and I_{peak}, indicating that this parameter alone does not fully determine the behavior of the focus, as diffraction becomes more and more significant at longer path lengths. However, the $10^{-10}\mathrm{m}^{1/3}$ $C_n^2 L$ threshold determined here is valid over the range of typical atmospheric turbulence strengths and for propagation distances up to 1 km.

In summary, we have performed experiments and simulations to assess the effect of realistic atmospheric conditions on mid-IR and long-wave-IR laser-induced avalanche breakdown for the remote detection of radioactive material. We find that strong turbulence reduces the number of breakdown sites in the focal volume by the fraction of the focal volume with an intensity above the breakdown threshold, but that a modest increase in laser energy can compensate for orders of magnitude increases in the turbulence level. Laser propagation simulations are in excellent agreement with these results, and provide code validation. Simulations of long-wave-IR ($\lambda = 10\,\mu$m) propagation through realistic turbulence suggest that avalanche-based remote detection of radioactive materials is robust, even in strong atmospheric turbulence conditions, up to ~ 0.5 km, and to well over 1 km for clear conditions. We also determined that the background seed density will be increased in areas of high aerosol concentration by measuring the background in the presence of $\sim$5 μm water droplets. However, even the highest aerosol densities in the typical range of atmospheric conditions are $<10\,\mathrm{cm}^{-3}$, many orders of magnitude less than the relevant seed densities induced by radioactive material and the cosmic-ray-generated background ion density. For this reason, it is unlikely that aerosols will have a significant effect on measurements in realistic outdoor conditions. While our results show promise for the remote avalanche-based detection of radioactive sources under realistic atmospheric conditions, future experiments at longer propagation ranges are needed; these will provide additional validation for simulations.

Funding. National Science Foundation (PHY2010511); The National Nuclear Security Administration'sOffice of Defense Nuclear Nonproliferation.

Acknowledgment. The authors thank R. Schwartz, I. Larkin, and E. Rockafellow for technical assistance.

Disclosures. The authors declare no conflicts of interest.

Data availability. The data underlying the findings of this study are available from the authors on reasonable request.

REFERENCES

1. D. Woodbury, R. M. Schwartz, E. Rockafellow, J. K. Wahlstrand, and H. M. Milchberg, Phys. Rev. Lett. **124**, 013201 (2020).
2. R. M. Schwartz, D. Woodbury, J. Isaacs, P. Sprangle, and H. M. Milchberg, Sci. Adv. **5**, eaav6804 (2019).
3. V. L. Granatstein and G. S. Nusinovich, J. Appl. Phys. **108**, 063304 (2010).
4. P. Sprangle, B. Hafizi, H. Milchberg, G. Nusinovich, and A. Zigler, Phys. Plasmas. **21**, 013103 (2014).
5. D. Kim, D. Yu, A. Sawant, M. S. Choe, I. Lee, S. G. Kim, and E. Choi, Nat. Commun. **8**, 15394 (2017).
6. D. Woodbury, R. M. Schwartz, and H. M. Milchberg, Optica **6**, 811 (2019).
7. G. Gbur and R. K. Tyson, J. Opt. Soc. Am. A **25**, 225 (2008).
8. W. Happer, G. J. MacDonald, C. E. Max, and F. J. Dyson, J. Opt. Soc. Am. A **11**, 263 (1994).
9. S. Lohani and R. T. Glasser, Opt. Lett. **43**, 2611 (2018).
10. T. Shirai, A. Dogariu, and E. Wolf, Opt. Lett. **28**, 610 (2003).
11. G. Andriukaitis, T. Balčiūnas, S. Ališauskas, A. Pugžlys, A. Baltuška, T. Popmintchev, M.-C. Chen, M. M. Murnane, and H. C. Kapteyn, Opt. Lett. **36**, 2755 (2011).
12. J. Isaacs, C. Miao, and P. Sprangle, Phys. Plasmas **23**, 033507 (2016).
13. W. Hoppel, *Atmospheric Electricity in the Planetary Boundary Layer* (National Academy Press, 1986).
14. I. Larkin, J. Griff-McMahon, A. Schweinsberg, A. Goffin, A. Valenzuela, and H. M. Milchberg, Opt. Lett. **45**, 2518 (2020).
15. S. Bendersky, N. S. Kopeika, and N. Blaunstein, Appl. Opt. **43**, 4070 (2004).
16. W. Nelson, J. P. Palastro, C. Wu, and C. C. Davis, J. Opt. Soc. Am. A **32**, 1371 (2015).
17. S. Kooij, A. Astefanei, G. L. Corthals, and D. Bonn, Sci. Rep. **9**, 6128 (2019).
18. D. C. Smith, J. Appl. Phys. **48**, 2217 (1977).
19. M. D. Feit and J. A. Fleck, Appl. Opt. **17**, 3990 (1978).
20. C. Macaskill and T. E. Ewart, IMA J. Appl. Math. **33**, 1 (1984).
21. V. I. Tatarskii, *Jerusalem: Israel Program for Scientific Translations* 1971 (1971).
22. D. G. Voelz, E. Wijerathna, A. Muschinski, and X. Xiao, Opt. Eng. **57**, 104102 (2018).
23. M. N. Polyanskiy, I. v Pogorelsky, M. Babzien, and M. A. Palmer, OSA Continuum **3**, 459 (2020).